GROUND-BASED HIGH SENSITIVITY RADIO ASTRONOMY AT DECAMETER WAVELENGTHS

P. Zarka*, J. Queinnec*, B. P. Ryabov†, V. B. Ryabov†,
V. A. Shevchenko†, A. V. Arkhipov†, H. O. Rucker‡, L. Denis§,
A. Gerbault§, P. Dierich¶, and C. Rosolen¶

Abstract

The decameter wave radio spectrum ($\sim 10 - 50$ MHz) suffers a very high pollution by man-made interference. However, it is a range well-suited to the search for exoplanets and the study of planetary (especially Saturnian) lightning, provided that very high sensitivity (~ 1 Jansky) is available at high time resolution ($0.1 - 1$ second). Such conditions require a very large decameter radiotelescope and a broad, clean frequency band of observation. The latter can be achieved only through the use of a broadband multichannel-type receiving system, efficient data processing techniques for eliminating interference, and selection and integration of non-polluted frequency channels. This processing is then followed by an algorithm performing bursts detection and measuring their significance. These requirements have been met with the installation of an Acousto-Optical Spectrograph at the giant Ukrainian radiotelescope UTR-2, and four observations campaigns of Jupiter, Saturn, and the environment of nearby stars (including 51 Peg and 47 UMa) have been performed in 1995–96. The scientific objectives, observation techniques, instrumentation, data processing and first results of these studies, as well as simulation results, are presented here. The sensitivity achieved ($3 - 6$ Jansky with $60 - 100$ msec integration time) is promising and should allow for planetary lightning detection and subsequent monitoring. Ground-based search for exoplanets at decameter wavelengths is shown to be a realistic program for stars closer than ~ 25 parsecs.

1 Introduction

The quest for life in the Universe is a major theme of modern astronomical research. It implies quite naturally the search for planets (beyond our solar system), which are considered as the most favourable place for the apparition of complex biochemical processes.

*DESPA, CNRS/Observatoire de Paris, F-92195 Meudon, FRANCE
†Institute of RadioAstronomy, Krasnoznamennaya 4, Kharkov 310002, UKRAINE
‡Space Research Institute, Halbaerthgasse 1, A-8010 Graz, AUSTRIA
§Station de RadioAstronomie de Nancay, USR B704, Observatoire de Paris, 18 Nançay, FRANCE
¶ARPEGES, CNRS/Observatoire de Paris, F-92195 Meudon, FRANCE

In addition, the existence of other "solar systems" is, as such, a fundamental question. This makes exoplanet search a subject where efforts and interest are rapidly growing.

Since the discovery of 51 Peg B in October 1995 [Mayor and Queloz, 1995], over 20 exoplanetary candidates have been discovered (of which 10 with mass $\leq 13 \times$ Jupiter's mass - see Schneider, [1997]), mainly via the detection of periodic oscillations of the parent star's spectral lines in response to the planet's orbital motion. Another successful method is pulsar timing, through which the first 3 exoplanets have been discovered ([Wolszczan, 1995], and references therein), and other methods include infrared imaging, astrometry, gravitational microlensing, etc.

The main difficulty for direct detection of an exoplanet is of course its relative proximity to its parent star and the highly unfavourable contrast between the electromagnetic output of the planet and that of the star: about 10^9 in the visible range and 10^6 in the infrared one. The low-frequency radio range is an exception, because the emissions are of nonthermal origin. In our solar system, for example, Jupiter's most intense magnetospheric radio bursts are frequently of higher intrinsic power than solar radio bursts in the decameter range (Figure 1). Four other magnetized planets (the Earth, Saturn, Uranus and Neptune) also produce very intense non-thermal auroral radio emissions, but at kilometer wavelengths due to the weaker magnetic fields of these planets, these emissions do not reach the ground because of the Earth's ionospheric cutoff below $\sim 5 - 10$ MHz. The decameter range ($\sim 10 - 30$ MHz) appears thus as a privileged range for direct detection of magnetized exoplanets through their magnetospheric (Jupiter-like) radio bursts. The example of Earth proves that "radio-planets" can orbit inside the circumstellar "habitability zone", so that the method described below does not exclude a-priori telluric, possibly habitable planets.

Three severe limitations must however be overcome in the decameter range, in order to assess the existence of radioemissions from magnetized exoplanets:

(i) the fluctuations of the sky (galactic) background, of very high brightness temperature $\sim 30000 - 50000$ K at 25 MHz,

(ii) the very poor angular resolution available ($\sim 1^\circ$ for a 1 km-diameter antenna), which implies high "confusion" during the observations (possible presence of other radiosources in the edges of the main radiotelescope lobe), and

(iii) intense variable interference (man-made, terrestrial lightning), up to 50 dB or more above the sky background fluctuations.

The first two ones require the use of a very large instrument (in terms of effective area and maximum extent). (iii) requires efficient interference elimination and burst detection algorithms.

A second target for high-sensitivity (~ 1 Jy level) decameter observations is the detection and possibly long-term study of solar system planetary lightning (from Saturn, but also Uranus, Mars or Venus). As shown below, this target requires a sensitivity $3 - 5$ times lower than exoplanet search, but as the signature of Jupiter's magnetospheric radio bursts

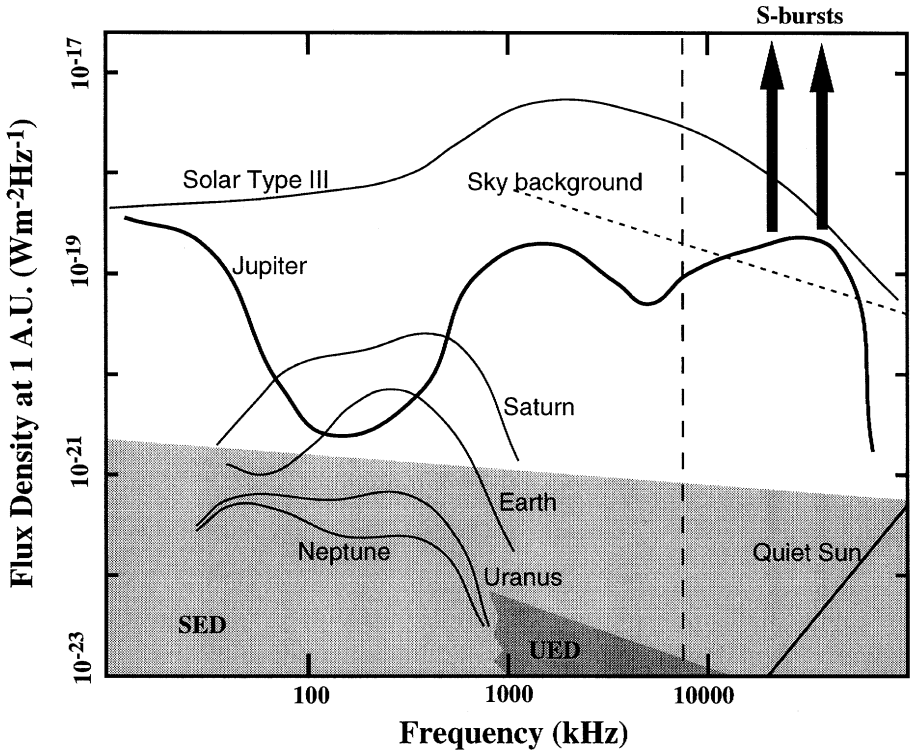

Figure 1: Comparative spectra of solar system radio emissions in the decameter-to-kilometer range, normalized to a distance of 1 A.U. (except for the sky background, [Kraus, 1986]). Average spectra of the auroral radio emissions of the five "Radio-planets" are displayed (adapted from Zarka, [1992]). That of Jupiter (boldface) is often as intense as solar type III radio bursts. Peak levels are about one order of magnitude above these averages. Jovian S-bursts fluxes can reach 10^{-16} *W* m^{-2} *Hz*$^{-1}$*. The grey-shaded regions labeled "SED" and "UED" (standing for Saturn/Uranus Electrostatic Discharges) show the range of intensities of these planetary lightning-associated radio emissions.*

and of planetary lightning is very similar with the observation parameters used, planetary lightning search represents a very good test bench on the way to radio-exoplanets discovery.

We summarize below the relevant properties of planetary lightning (section 2) and of magnetospheric (Jupiter) radio bursts (section 3). We extrapolate the latter in a both optimistic and realistic way, deduce constraints for detectability in terms of sensitivity (section 4). Temporal broadening and dispersion problems are also discussed. The instruments and observation procedure are described in section 5, and the method of analysis in section 6, as well as simulation results. Preliminary results of the first observation campaigns are presented in section 7.

2 Saturn's and other Planetary Lightning

Saturn's lightning-associated radio emission, coined SED for "Saturn Electrostatic Discharge" when discovered by the Voyager 1-Planetary Radio Astronomy experiment, was

observed for one week around Voyager 1 and 2 encounters with the planet in 11/1980 and 8/1981 [Kaiser et al., 1984]. Characteristic physical properties of these emissions are [Zarka and Pedersen, 1983; Zarka, 1985a,b]:

- a typical duration per event of 30 to 300 msec,
- a broadband smooth spectrum ($\leq$ 20 kHz to $\geq$ 40 MHz), decreasing by less than one order of magnitude over this range, with an instantaneous spectral power between 0.1 and 100 W Hz^{-1}, corresponding to flux densities of $0.4 - 400$ Jy (1 Jy = 1 Jansky = 10^{-26} W m^{-2} Hz^{-1}) at the Earth (Figure 1),
- an occurrence of 15 events/minute (for Voyager 1) to $\sim$ 4 events/minute (for Voyager 2), also evidencing the large variability of this phenomenon on the timescale of months.

During the Voyager 1 encounter with Saturn, typically more than 1 event per minute was detected with a duration $\geq$ 30 msec and flux $\geq$ 50 Jy (at the Earth, i.e. at $\sim$ 10 A.U. distance), and $> 7 - 8$ events per minute with a flux $\geq$ 5 Jy.

Similar broadband emissions were detected by Voyager 2 during its encounter with Uranus in 1986 [Zarka and Pedersen, 1986], with a steeper spectrum in $\sim f^{-1}$ and a weaker intensity, from 10^{-22} to 10^{-24} W m^{-2} Hz^{-1} at 1 A.U. distance, i.e. 0.25 to 25 Jy as observed from the Earth ($\leq$ 2.5 Jy above 10 MHz - see Figure 1).

Saturn's lightning -and marginally Uranus' ones- are thus ideal targets for high-sensitivity radio observations at the Jansky level. This is not the case for Neptune, where only a few weak events were marginally detected by Voyager 2 [Kaiser et al., 1991]. The case of Venus is more interesting, with indirect, controversial evidences for the presence of lightning (from optical, radio and plasma waves observations - see Zarka et al., [1992], and references therein). Finally, Martian lightning have never been detected, but only little searched for, although dust charging and large scale electric fields build-up is not excluded. These last two targets are far from uninteresting, even if lightning-like activity is weak, because of their proximity.

3 Magnetospheric Radio Bursts

3.1 Nonthermal Planetary Radio Emissions & Jovian S-bursts

As shown in Figure 1, auroral planetary low-frequency radio emissions [Zarka, 1992] are far more intense than radio emissions from the quiet Sun in the same range [Boischot and Denisse, 1964], and Jovian decameter emissions are as intense as the most intense solar (Type III) bursts in the decameter range [Lecacheux et al., 1989]. Moreover, the part of the Jovian decameter activity known as "millisecond" or "S" bursts (see Zarka et al., [this volume], and references therein) can reach flux densities two orders of magnitude higher than Jupiter's slowly variable radio component, up to 10^{-16} W m^{-2} Hz^{-1} at 1 A.U. distance, the emission drifting over several MHz total band during a few tens of msec.

They are thus the most intense decameter radio component originating from the solar system. However, as shown in the next section, Jovian S-bursts are not detectable on the sky background fluctuations beyond a few tenths of a parsec, even with the largest existing decameter radiotelescope. To estimate what we can expect from nonthermal radio emissions of extrasolar planets, we have to rely on the present theoretical understanding of solar system planetary radio emissions.

Auroral radio emissions are attributed to Cyclotron-Maser radiation of unstable electron populations of a few keV energy, precipitating along converging field lines at high magnetic latitude [Le Quéau, 1988; Louarn, 1992]. The radio emission is produced along auroral magnetic field lines near the local electron gyrofrequency, and is circularly or elliptically polarized. Auroral radio emissions are ubiquitous in the solar system, and the five strongly magnetized planets are all powerful radiosources. Moreover, part of the emission is produced under the form of powerful radio bursts at all the "Radio- planets" [Zarka, 1992]. It is also worth noting that for the four giant planets, the observed intensities are strongly modulated at the planetary spin period by the rotation of the magnetic field.

3.2 How Strong Planetary Radio Bursts Can Be?

Based on the Cyclotron-Maser theory, Le Quéau et al. [1985] and Zarka et al. [1986] have modelled the intensity of the Earth's auroral kilometric radiation, and Galopeau et al. [1989] have given a theoretical explanation for the spectrum of Saturn's kilometric radiation. These results can be extrapolated to all the radio planets, and in spite of the incomplete state of the theory of planetary radio emissions generation (the origin, acceleration, and distribution function of the radiating electrons are still unclear, as well as the origin of the fine structures of auroral radio emissions in the frequency- time plane), interesting scaling laws can be drawn from solar system radio planets:

- Desch and Kaiser [1984] and Zarka [1992] have shown that the auroral radio output (P_r) of the Earth, Jupiter, Saturn, Uranus and Neptune is well correlated ($> 99\%$) to the solar wind input (P_i) on each magnetosphere's cross-section, and approximately proportional to it. P_i is easily shown to be proportional to $N_0^{2/3} V^{7/3} B_0^{2/3} D^{-4/3}$, where N_0 is the solar wind density at 1 A.U., V the solar wind bulk velocity, B_0 the planetary dipole moment, and D the planet's orbital radius.
- In addition, Zarka [1992] has suggested another cause for controlling the auroral radio output of a magnetized planet: the homogeneity $\Lambda = L_B/\lambda$ of the auroral source region, where L_B is the source magnetic field gradient length and λ the emitted wavelength. It has been shown that Λ varies as $B_0 R_p$ (with R_p the planetary radius), is well correlated to P_r ($> 93\%$ for the 5 magnetized planets, $> 99.9\%$ for Jupiter, Saturn and the Earth only) and again approximately proportional to it (within a factor $2\times$).

Finally, P_r is proportional to

$$P_r \approx N_0^{2/3} V^{7/3} B_0^{5/3} (1/D)^{4/3} R_p \qquad (1)$$

We can use this relation to draw estimates for the auroral power that can be radiated by a "radio- exoplanet", as compared to Jupiter:

- R_p can only be increased by a small factor with respect to the Jovian radius (smaller than $\times 5$) before the corresponding planet reaches the lower limit of stellar sizes and masses [Zombeck, 1990].
- Of the presently 8 confirmed exoplanets (Schneider, 1997), 3 have a semi-major axis ≤ 0.05 A.U. (around 51 Pegasi, τ Bootes and υ Andromeda - see Baliunas et al., [1997]). A gain of a factor 20 on $1/D$ is thus not unreasonable.
- The planetary dipole moment B_0 cannot be increased by more than a factor ≈ 2 without shifting the radio emission peak in the meter range.
- While stellar winds velocities V are confined within a factor ≈ 3 (higher or lower) of the solar wind speed at the Earth orbit (≈ 400 km s^{-1}), massive hot stars can have a mass-loss rate $(N_0 m_p/D^2)VD^2 \geq 10^7$ times the solar one [Zombeck, 1990; Lang, 1991]. As high density winds are generally slower, $N_0^{2/3}$ can thus be increased by up to $(1/3 \times 10^7)^{2/3} \approx 10^5$ as compared to the solar system's case. The influence of solar wind fluctuations (especially density and pressure) on Jupiter and Saturn's auroral radio outputs has been demonstrated [Barrow et al., 1986; Zarka and Genova, 1989; Rucker et al., 1989, and references therein], although it cannot be guaranteed that P_r remains proportional to $N_0^{2/3}$ in variations over several orders of magnitude. Furthermore, at Jupiter, the solar wind control is negligible for radio emissions generated through the electrodynamic interaction Io-Jupiter, as the S-bursts [Genova et al., 1987]. "Usual" auroral emissions being ~ 2 orders of magnitude less intense than S-bursts (Figure 1), a more conservative factor for the gain in radio radiated power than can be expected from a denser stellar wind surrounding the planet is $\approx 10^2 - 10^3$.

Combining the above factors in the most favourable way, one gets an upper limit of the radiated auroral power of a "radio-exoplanet": $\approx 10^2 - 10^3 \times 1^{7/3} \times 2^{5/3} \times 20^{4/3} \times 5 = 8 \times 10^4 - 10^5$ (where the estimated influence of the stellar wind density and velocity are merged within the factor $10^2 - 10^3$) times the Jovian maximum radio output at decameter wavelengths (S-bursts). Such a high value is probably not reached very often, and a factor $\approx 10^3$ is probably reached more commonly.

Let us remark here that S-bursts may at first seem exceptional because they depend on the Io-Jupiter coupling, but they are attributed to the same (Cyclotron-Maser) microscopic generation mechanism -the discrete nature of bursts is rather attributed to the way electrons are accelerated in the Io-Jupiter circuit-, the other solar system radio-planets also produce intense bursts, and the interaction between an ionized body (Io's ionosphere, which takes origin primarily in the tidal stresses exerted by Jupiter on Io) and a planet's (Jupiter's) rapidly rotating magnetic field may be as common as the simple existence of strongly magnetized Jovian-like planets.

4 Detectability

4.1 Sensitivity

We note I_J the intensity -normalized to 1 A.U.- of the most intense Jovian magnetospheric bursts (S-bursts, of flux $\approx 10^{-16}$ W m^{-2} Hz^{-1}), and α a multiplying factor in the limits discussed above. The maximum distance d_{max} (in parsecs, with 1 pc $= 2 \times 10^5$ A.U.) at which a radioemission of intensity αI_J can be detected with a Signal/Noise ratio of N is:

$$d_{max} = 5 \cdot 10^{-6} \times (\alpha I_J A_e / 2NkT_s)^{1/2} (\delta f \delta t)^{1/4} \quad (2)$$

where A_e is the radiotelescope effective area, T_s the sky background temperature (30000 to 50000 K depending on the direction of observation - see e.g. Kraus, [1986]), and δf and δt the spectral band and integration time of observation. The noise level is defined by the fluctuations of the sky (galactic) background, of amplitude

$$\sigma_s = 2kT_s / A_e (\delta f \delta t)^{1/2} \quad (3)$$

For $\alpha = 1$ (Jupiter), $N = 2.6$ ($> 99\%$ confidence level), $\delta t = 1$ s, $\delta f = 30$ kHz (typical integration time and bandwidth for Jovian decameter observations), and $A_e \approx 5000$ m^2 (effective area of the Nançay decameter array, France, [Boischot et al., 1980b]), we obtain $d_{max} \approx 0.03$ pc, which is extremely small. Even for $\alpha = 10^3$, d_{max} is still only about 0.9 pc, which is smaller than the distance of the nearest star (α Cen at 1.3 pc). Obtaining $d_{max} = 1$ pc with $\alpha = 1$ requires a radiotelescope effective area $A_e = 6$ km^2 all other parameters remaining unchanged, but there exists no instrument of that size. With $\alpha = 10^3$, $d_{max} = 5$ pc is obtained with an effective area about 170000 m^2, which is still too large. As the integration time δt must remain $\leq 50 - 300$ msec for not diluting lightning or magnetospheric bursts radio emission, it appears that both a very large instrument and broad bandwidth are required to achieve high-sensitivity observations.

The only decameter radiotelescope with an adequate area is the UTR-2 array, in Kharkov (Ukraine, [Braude et al., 1978]), with a physical area of 140000 m^2. Taking $A_e = 50000$ m^2 (see section 5.1 below), $\alpha = 10^3$ and $\delta t = 300$ msec, $d_{max} \geq 5$ pc implies $\delta f \geq 1.1$ MHz. Table 1 summarizes the sensitivity (σ_s in Jy) for $\delta t = 50 - 300$ msec and $\delta f = 3 - 6$ MHz (i.e. $\delta f / f = 0.1 - 0.2$ at the frequency of observation ~ 30 MHz), and the corresponding maximum range of detectability d_{max} for $\alpha = 1$, 10^3, and 10^5. It shows that exoplanet search at decameter wavelengths is very realistic up to distances of $5 - 10$ pc, and still feasible up to 25 pc.

Table 1 also shows that the Jansky-level sensitivity is achieved with integration time about 0.3 s and a clean bandwidth of a few MHz. However, as the decameter range is very severely polluted -mainly due to man-made radio frequency interference (or RFI, [Erickson, 1990; Gérard, 1993]), it is necessary to divide the spectral band of observation in numerous narrowbanded channels, and to reconstruct a broad clean band after elimination of interference. If a broad band is directly recorded, RFI, which can be up to $40 - 50$ dB above the signal searched for, will entirely dominate the receiver's output and prevent any detection of weak signals.

Table 1: Sensitivity (σ_s) and maximum range of detectability ($d_{max} = 5 \cdot 10^{-6} \times (\alpha I_J / N\sigma_s)^{1/2}$) as a function of integration time δt, bandwidth of observation δf and scaling factor α.

δt (msec)	δf (MHz)	σ_s (Jy)	d_{max}(pc)		
			$\alpha = 1$	$\alpha = 10^3$	$\alpha = 10^5$
50 (lightning observations or search for very short-lived radio bursts)	3	5.7	0.13	4.1	13.0
	6	4.0	0.16	4.9	15.5
300 (exoplanet search)	3	2.3	0.20	6.5	20.5
	6	1.6	0.25	7.8	24.5

4.2 Temporal Broadening and Dispersion

Low-frequency radio signals propagating in a plasma (interplanetary or interstellar) suffer several effects (scattering and diffraction causing scintillations, broadenings and time delays). For broadbanded short-lived bursts of interest here, the main two perturbating effects are dispersion and temporal broadening [Cordes, 1990].

The frequency-dependent time delay causing dispersion writes, for two frequencies f_1 and f_2:

$$t(f_1) - t(f_2) = 4.15 \times 10^6 DM(f_2^{-2} - f_1^{-2}) \quad (4)$$

with t in msec, f in MHz, and DM being the dispersion measure in pc cm^{-3}. The temporal broadening τ varies in $f^{-22/5}$ (Kolmogorov scaling - see Cordes, [1990]).

In the solar system, assuming that solar wind density decreases in $1/D^2$ from a typical value $N_0 = 10$ cm^{-3} at the Earth orbit, we derive a dispersion measure $DM \leq 10$ AU cm^{-3} $= 5 \times 10^{-5}$ pc cm^{-3}. The resulting dispersion is negligible (≤ 0.3 msec between 20 and 30 MHz, to ≈ 1.5 msec between 10 and 20 MHz). The corresponding temporal broadening is also very weak, less than a msec at decameter wavelengths.

For the nearby stars, targets for radio-exoplanet search, DM is of the order of a few pc cm^{-3}. Table 2 lists time delays and broadenings for $DM = 1$ pc cm^{-3} and $DM = 10$ pc cm^{-3}, and for frequencies 20, 25 and 30 MHz. Arrival times of waves emitted simultaneously at 20 and 30 MHz differ by 5.8 s for $DM = 1$ pc cm^{-3}, and are proportional to DM. De-dispersion must thus be introduced (according to Eq. [4]) when integrating numerically the dynamic spectra after interference elimination. In our frequency and distance ranges of interest, the temporal broadening is equal to a few tens of msec. A shorter integration time for data acquisition is then useless. As shown below, we have used $\delta t = 300$ msec for exoplanet search, which suppresses the problem of temporal broadening.

Table 2: Time-delays and broadenings of radio spikes versus frequency and dispersion measure.

	DISPERSION Time delay (sec) [wrt $f = \infty$]		TEMPORAL BROADENING (msec)	
Frequency (MHz)	for DM (pc cm^{-3})		for DM (pc cm^{-3})	
	1	10	1	10
20	10.4	104	19	119
25	6.6	66	7	45
30	4.6	46	3	20

5 Instruments and Observations

5.1 The UTR-2 array

The UTR-2 array of the Kharkov Institute of Radio Astronomy (E. Long. = 36°56', Lat. = 49°38' - see Braude et al., [1978]) is the decameter radiotelescope with the largest physical area in the world. It is a phased array of 2040 thick dipoles (1.8 × 8 m) arranged in T-shape: 600 dipoles in a 900 m × 50 m East-West branch, and 1440 dipoles in a 1860 m × 50 m North-South branch. The total physical area is 138000 m^2. It operates between 7 and 35 MHz, with a peak sensitivity about 20 MHz. All the dipoles are aligned in the EW direction, along which UTR-2 is thus polarized. UTR-2 (like the Nançay decameter array) has no mobile part, and pointing is achieved through phasing, computer- controlled delays and summation of groups of antennas, independently for the EW and NS branches. Five summations are actually performed in parallel, so that each branch has a 5-beam pattern on the sky (with one output per beam). Beams of the NS branch are 14° × 30' at 25 MHz (elongated in the EW direction) and separated by 30' intervals along the NS direction. Beams of the EW branch are 14° × 1° at 25 MHz and separated by 1° intervals (in EW). It is in principle possible to correlate any of the 5 EW outputs to any of the 5 NS ones, to synthezise one of 25 pencil beams (1° × 30').

Calibrations of the radiotelescope effective area through observations of the Cas A supernova remnant give $A_e \approx 50000 - 60000$ m^2 for the NS branch (for a source in the meridian plane), and twice less for the EW branch.

5.2 The Acousto-Optical Spectrograph

The receiver used is an Acousto-Optical Spectrograph (AOS, [Raterron, 1985; Abada-Simon, 1990]), built in Meudon-Nancay and installed at UTR-2. It is a multichannel-type receiver, performing acquisitions of a 26 MHz band centered on 40 MHz in 877 channels simultaneously. The 26 MHz band of observation is selected via a HF interface (performing frequency shift in the band 40 ± 13 MHz, amplification and filtering) and sent to the AOS. A piezo-electric transducer converts the radio signal into acoustic waves injected in a crystal (Bragg cell) where they create stationary patterns of optical indices variations. There patterns are used as diffraction gratings to disperse and deviate a Laser

beam sent through the crystal, proportionally to the frequency of each acoustic wave present in the Bragg cell. The spectrum of the incident radio signal is thus converted to a linear distribution of Laser light, detected by a 1D CCD. The latter is computer-controlled and -read, and spectra are recorded (on a PC) after integration with $\delta t \geq 5$ msec (no upper limit).

The channels are linearly spaced every ~ 30 kHz, but the diffraction spots -due to the AOS optical processor- falling on the CCD create broad low-intensity wings, so that the Noise Equivalent Band of each channel is ~ 130 kHz. The AOS dynamic range is ~ 25 dB. External attenuators allow to increase the total dynamic range of observations, but remain constant during an acquisition sequence (12 to 45 minutes, see below). If saturating interference occurs during an acquisition, the whole spectra recorded during its occurrence are spurious (not only the frequencies where the interference occurs) because high-intensity acoustic waves generate non-linearities in the crystal response and perturbate the acousto-optical interaction. The corresponding spectra must then be discarded during the post- processing. The second weakness of AOS receivers is their stability: it remains better than $\sim 1\%$ for no longer than a few tens of seconds, and $\leq 2-3\%$ for a few minutes. This is an additional (technical) motivation for the search for short-lived bursts, because fluctuations slower than a few seconds (either due to the AOS drift or to ionospheric scintillations) can be filtered before burst detection.

5.3 Observation Procedure

We have taken advantage of the multi-beam capability of UTR-2, using a special HF interface shifting the same 10 MHz band from two different beams **simultaneously** in the lower and upper half of the AOS 26 MHz band. One beam ("ON") is pointed to the target radiosource (Saturn or a nearby star), while the other one ("OFF" or reference beam) is pointed 1° away from the "ON" beam (see Figure 2). Each 10 MHz band is recorded in 333 frequency channels. The selected integration time is $60-100$ msec/spectrum for Saturn's lightning observations, and $\sim 250-270$ msec/spectrum for exoplanetary radio bursts search (see Table 3). One observation consists of the acquisition of 10000 consecutive spectra, for 12 to 45 minutes and a data volume ≈ 20 Mbytes. Data are stored on tapes or CD-Rom, for post-processing on a workstation.

Although radioastronomical observations can be in principle performed 24 hours a day, they are of much better quality at night ($\sim$ 0h to 5h Local Time) in the decameter range, due to a much lower level of man-made RFI (industry, radio broadcasting, amateur emitters, radars, etc., [Denis and Zarka, 1996]). Observations for a given radiosource are carried on preferably around the meridian transit, corresponding to maximum elevation and thus better immunity to interference -especially propagating by reflection under the ionosphere-, and to a less distorted radiotelescope lobe reducing the confusion. The NS branch of UTR-2 was mostly used, due to (i) its larger effective area and (ii) its lowest susceptibility to strong interference generated by emitters located to the South and entering the southern part of the EW lobe. A few tests have also been performed in correlation mode (NS×EW).

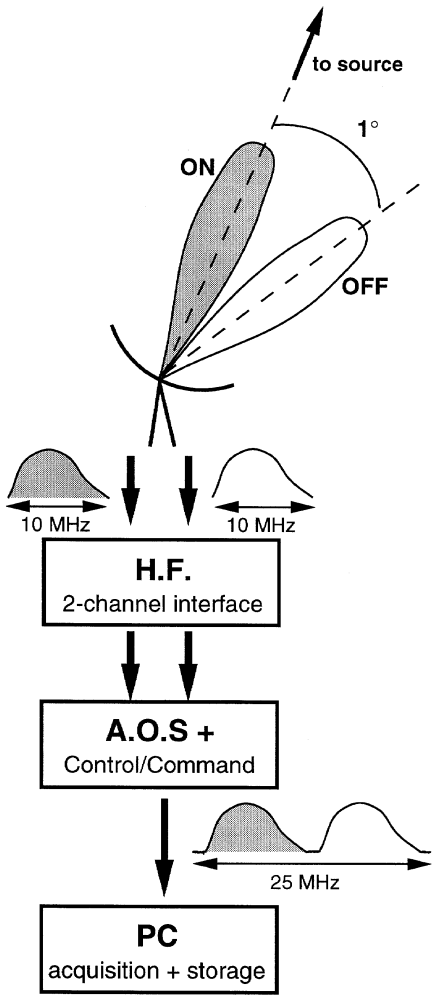

Figure 2: Sketch of the observing scheme at UTR-2 radiotelescope. See section 5 for details.

5.4 Observation Campaigns

Table 3 summarizes the high-sensitivity observations performed during the five campaigns that have taken place in 1994–96. Observations during the first campaign (February 1994) were very preliminary: a swept-frequency analyzer was used for Saturn observations ($\delta f = 100 - 300$ kHz, $\delta t = 10$ sec per 400-channel-spectrum, i.e. dwelling for 25 msec on each frequency channel), and nearby stars observations were performed with one ON beam only. Simultaneous ON/OFF observations were carried on during the four subsequent campaigns (1995–96).

Targets for exoplanet search (in addition to the stars around which planets have already been found) were selected according to the following criteria: proximity, single star, declination $\geq -10°$ in order to reach a high elevation near the meridian transit (except Gliese 229, around which a brown dwarf has been detected), excess of Infrared radiation, and possible presence of a circumstellar disk. In addition, ϵ Eri has been a favoured SETI target for several years. A stellar spectral type close to the Sun's one is preferable (G, K), but the statistical dominance of dwarf stars (M type) in the solar neighbourhood

Table 3 : *Observations campaigns at UTR-2, 1994-1996.*

Observation campaign (*)	Target Name	Spectral type	Distance (pc)	Coordinates α h m s	(1950/2000) δ ° '	number of acquisition sequences	Acquisition duration (minutes)	Time resolution (seconds per spectrum)	Comment
#1	Saturn	-	5×10^{-5}	-	-	3	~150	10	Swept-frequency Analyzer
#1	Wolf 359	dM8e	2.4	10 54 06	+07 19	4	20	0.5	ON beam only
#1	ε Eri	K2V	3.3	03 30 36	-09 38	2	20	0.5	ON; Circumstellar disk ? IR excess
#1	Ross 128	dM5	3.3	11 45 06	+01 06	1	20	0.5	ON; Circumstellar disk ?
#1	Ross 614	dM7e	4.1	06 26 48	-02 46	2	20	0.5	ON; Binary
#2	Venus	-	$\sim3\times10^{-6}$	-	-	1	15 - 30	0.25 - 0.5	ON/OFF
#2	Saturn	-	5×10^{-5}	-	-	14	12 - 18	0.06 - 0.1	ON/OFF beams
#2	Barnard	M5V	1.8	17 55 24	+04 33	1	15 - 30	0.25 - 0.5	ON/OFF
#2	BD +36°2147	M2V	2.5	11 00 36	+36 18	2	15 - 30	0.25 - 0.5	ON/OFF; IR excess
#2	Ross 248	dM6e	3.2	23 39 24	+43 55	1	15 - 30	0.25 - 0.5	ON/OFF
#2	BD +50°1725	K7V	4.5	10 08 18	+49 42	3	15 - 30	0.25 - 0.5	ON/OFF; IR excess
#2	BD +68°946	M3.5V	4.7	17 36 42	+68 23	4	15 - 30	0.25 - 0.5	ON/OFF
#2	BD +43°4305	dM5e	5	22 44 42	+44 05	5	15 - 30	0.25 - 0.5	ON/OFF
#2	Altaïr	A7IV,V	5.1	19 48 18	+08 44	2	15 - 30	0.25 - 0.5	ON/OFF; IR excess
#2	BD +15°2620	M4V	5.2	13 43 12	+15 10	8	15 - 30	0.25 - 0.5	ON/OFF; IR excess
#3	Gliese 229	M1/M2V	6	06 10 35	-21 51	3	45	0.27	ON/OFF; Brown Dwarf †
#3	51 Peg	G2IV	14.7	22 57 27	+20 46	14	45	0.27	ON/OFF; Planet †
#3	Gliese 9245	G8V	19	07 52 03	-01 17	7	45	0.27	ON/OFF; Decameter radiosource GR 0752-01
#4	47 UMa	G0v	13.3	10 59 29	+40 26	5	43	0.26	ON/OFF; Planet †
#5	Saturn	-	5×10^{-5}	-	-	58	12 - 18	0.06 - 0.1	ON/OFF beams
#5	Gliese 229	M1/M2V	6	06 10 35	-21 51	9	45	0.27	ON/OFF; Brown Dwarf †
#5	51 Peg	G2IV	14.7	22 57 27	+20 46	30	23 - 45	0.14 - 0.27	ON/OFF; Planet †

(*) #1 = 31/1 - 5/2/1994; #2 = 13-17/5/1995; #3 = 13-16/11/1995; #4 = 14/3/1996; #5 = 8-16/10/1996.
(†) Companion previously detected by spectroscopic techniques (radial velocity, spectral lines).

($\leq$ 10 pc) leaves little choice for this last criterion. Flaring red dwarves must be avoided, because they could produce radio bursts of the kind searched for revealing planetary companions (see section 8). Most of the data are still being analyzed. Preliminary results are reported in section 7.

6 Method of Analysis

6.1 Interference Elimination and Bursts Detection

One acquisition consists of a pair of frequency-time arrays (10 MHz $\times$ 12 to 45 min) recorded simultaneously from the ON and OFF beams. These dynamic spectra are severely contaminated, even in the nighttime, by two main types of interference: terrestrial lightning and man-made signals. The former are broadbanded spikes, intrinsically $\sim 10^4$ times weaker than Saturnian lightning [Zarka et al., 1995], but detected -due to their proximity- at a level several tens of dB above that expected for Saturnian lightning or exoplanetary radio bursts. The latter are due to local emitters operating also on the nighttime (radars, amateurs -Citizen Band $\sim$ 27 MHz-, etc.) or to remote emitters whose signals are received after multiple reflexions under the ionosphere; they are generally of narrower bandwidth, semi-permanent or of short duration, and very intense. All these spurious signals must be identified and eliminated in order to reconstruct a broad clean band. Frequency integration (over δf) should then increase the S/N ratio proportionally to $\delta f^{1/2}$. The difficulty of the task can be compared to that of the detection of individual pulsar signals in the decameter band, without accumulation of many pulses (see e.g. Manchester and Taylor, [1977]). Although much work has been done on interference immunity, real-time processing of narrowband observations, and post-processing of radio maps (at meter wavelengths and shorter), very few results are reported, to our knowledge, on the processing of broadband dynamic spectra (see e.g. the *Proceedings of the NRAO workshop "Interference identification and excision", Green Bank, 1982*, & the *Abstracts of the U.R.S.I. Symposium "Interference problems in Radio Astronomy and Communications - or Cosmic Ecology", XXVth General Assembly, Lille, France, pp. 746-753, 1996*). The simultaneity of ON and OFF observations is obviously a decisive advantage of our observation procedure, because many of the above interference enter both beams and are thus correlated in the ON and OFF dynamic spectra.

We have developed a procedure of analysis involving the following steps for each acquisition:

(1) Pre-processing, to prepare the data for identification of interference and signal detection.

(2) Interference identification, through local and global frequency-time statistical analysis of dynamic spectra, together with high-pass filtering of the data.

(3) Tests of signal "gaussianity" which justifies and measures the quality of step (2).

(4) Frequency integration and signal detection (broadband spikes) over the noise background.

The detailed procedure is as follows:

(1.1) Identification of pointing times. The main beam of UTR-2 is pointed to the source every 2 minutes, which involves different phasing and delays for the antenna groups. This generates a strong spurious RFI for a few hundred msec and may lead to variations of the background level. 2-min. intervals between pointings (interpointing sequences) are generally processed independently (see below).

(1.2) Correction for the frequency response of UTR-2 (antennas, amplifiers, losses in cables ...) + AOS, and of the sky background (cf. Figure 1), in order to obtain flat ON and OFF dynamic spectra. We first neglect the presence of RFI. The raw spectrum $I(f,t)$ can be written:

$$I(f,t) = G(f,t) \times [S(f,t) + s(f,t)] + N(f,t) \tag{5}$$

where G, S, s and N are respectively UTR-2's gain, and the spectra of the sky background, the signal searched for, and the system noise. We perform time-averaging, to obtain:

$$\begin{aligned} < I(f,t) >_t &= < G(f,t) >_t \times < S(f,t) + s(f,t) >_t + < N(f,t) >_t \\ &\approx G(f) \times S(f) + N(f) \end{aligned} \tag{6}$$

because G, S and N are not expected to vary during an acquisition, and $< s(f,t) >_t$ is negligible because we look for weak sporadic signals. From [5] and [6], it comes:

$$\begin{aligned} I(f,t)/ < I(f,t) >_t &= 1 + G(f) \times s(f,t)/[G(f) \times S(f) + N(f)] \\ &= 1 + s(f,t)/[S(f) \times (1 + \alpha(f))] \end{aligned}$$

where $\alpha(f)$ stands for the ratio N/GS, and would be equal to 0 in the absence of system noise. In practice α is always ≤ 1 at UTR-2 (Braude et al., 1978). Finally, the spectral "flattening" of the dynamic spectra is performed as:

$$I(f,t)_{flat} = (I(f,t)/ < I(f,t) >_t - 1) \times S(f) = s(f,t)/(1+\alpha) \tag{7}$$

The resulting signal $I(f,t)_{flat}$ has a zero time-average and $(1+\alpha)$ is a weighting factor $(1 < (1+\alpha) \leq 2)$ that favours the parts of the spectrum where the system noise is minimal.

(1.3) Elimination of the frequency channels with average intensity lower than a specified threshold (typically 5 dB below the peak value of an average spectrum). The corresponding channels bring an additional contribution to the noise level, but almost none to the signal.

(1.4) Elimination of spectra containing signal close to saturation (cf. section 5.2).

(2.1) The basic idea underlying interference identification is that, due to their intensity much higher than sky background fluctuations and expected signal levels, interference can be localized in time and frequency (in a map of bad pixels) using statistical analysis of the distribution of amplitudes in the dynamic spectra. This is done by computing amplitude distributions over different time intervals and using various moments of these distributions to detect anomalously high values associated with interference. Inspection of dynamic spectra reveals three relevant timescales to be used for this analysis: 1 to 3 consecutive spectra (spikes), a few seconds (intermittent interference), and ≥ 2 minutes.

(2.2) In addition, cross-correlation of ON and OFF dynamic spectra are used to further identify spurious signals, often present in both.

(2.3) Moreover, we designed a specific high-pass filtering procedure which uses the information about interference position in the frequency-time plane and interpolates across the polluted areas. The filtering is aimed to remove background variations slower than ~ 1 second, due to variations of the telescope radiation pattern from pointing to pointing, and propagation effects through the ionosphere.

(2.4) As the flattening, filtering and statistical interference identification are interdependent, the whole process is iterated (2 times total) for better performance. Remaining individual high-intensity pixels are then removed. The final output consists of ON and OFF flattened, filtered dynamic spectra and a map of the interference ($m(f,t)$).

(3) Two tests are used to quantify the efficiency of the above "cleaning" procedure: (i) a test of "gaussianity", studying the distribution of fluctuations of coarse-grained dynamic spectra (with frequency resolution δf) versus δf (dispersion is expected to decrease in $\delta f^{-1/2}$ for gaussian noise fluctuations, according to Eq. [3]), independently in ON and OFF channels, and (ii) residual correlation of ON and OFF dynamic spectra versus δf (expected to be ≈ 0 after interference elimination).

(4.1) The two dynamic spectra (output of step (2)) are integrated in frequency after removing the interference defined by the map, according to the following formula:

$$I(t) = \frac{\sum_f m(f,t) \times I(f,t)}{\sum_f m(f,t)} \times \frac{\left(\sum_f m(f,t)\right)^{1/2}}{< \left(\sum_f m(f,t)\right)^{1/2} >_t} \equiv I_0 \times C \qquad (8)$$

In Eq. [8], the term I_0 is simply the averaging over the clean part of each spectrum, while C is a correction term compensating for the variable number of clean channels in each spectrum, to obtain a constant dispersion in the final time series $I(t)$. This is done for both ON and OFF dynamic spectra, so we obtain two time series used for final burst detection.

(4.2) Broadband bursts should appear as high intensity values in the "ON" time series. To detect them, we compare the high-value tails of statistical distributions of ON and OFF time series. The discriminating statistics we use as evidence for the presence of signal are:

(a) number of peaks higher than N $\times \sigma$ level (typically $N = 3$) for ON and OFF time series.
(b) number of ON peaks higher than N $\times \sigma$ level and higher than twice the corresponding OFF level, and same with ON and OFF exchanged.
(c) same for differences (ON minus OFF and OFF minus ON) series.
(d) asymmetry of ON and OFF intensity distributions.

(4.3) We check for the broadbandness of the detected signals by plotting the smoothed spectra of the detected peaks in time series. We also perform step (4) after dividing the band of observation in two equal bands (a few MHz each) and considering as significant only the signals which are detected in both bands.

6.2 Simulation and Performances

Simulations have been performed to test the above procedure. In the one presented here (Figure 3), ON and OFF dynamic spectra have been built containing 6 consecutive panels of 1000 spectra $\times$ 200 frequency channels each, simulating 12 minutes of observation with time resolution 120 msec/spectrum and 6 MHz total bandwidth (Figure 3a). Each panel contains gaussian noise with average = 1. and RMS dispersion $\sigma = 0.01$ (consistent with that of observations with 120 msec resolution). In addition, panels 2, 4, 5 and 6 contain simulated interference: 20 polluted frequencies with fluctuating intensity of average $1 - 10\sigma$; 100 intermittent interference with intensity $1 - 10\sigma$, each covering areas of $1-5$ frequency channels $\times 10-100$ spectra, and a 100 pixel-long drifting structure. Also, panels 3 to 6 contain a 15 broadband spikes each covering part of one spectrum ($80 - 200$ frequency channels) with fluctuating intensity $\sim 0.6 - 3\sigma$. Interferences are generated randomly (but with the above characteristics, which mimic realistically observed RFI) and independently in each panel of ON and OFF dynamic spectra, except for the broadband spikes whose position is correlated in ON and OFF. Lightning-like (or burst-like) signal is simulated in panels 3 to 6 only as broadband spikes present in the ON dynamic spectrum only but with much weaker intensity than interference ($0.2 - 1\sigma$, too weak to be seen on Figure 3a). Finally, the strong spurious RFI linked to pointings are added at the edges of each panel, and an overall linear (resp. sinusoidal) variation of the background level of 20% total amplitude is superimposed on panel 5 (resp. 6) of each dynamic spectrum. On the 1.2×10^6 pixels of each dynamic spectrum, about 1.4×10^5 are polluted by interference (or about 12%, with 4×10^4 spurious pixels in common in ON and OFF dynamic spectra, and thus $\sim 2.4 \times 10^5$ bad pixels for ON and OFF taken together). In comparison, only ~ 8000 pixels enter in the composition of the weak signals searched for.

These simulated data have then been processed like real ones (following section 6.1). Step (1.1) is illustrated in Figure 3b (for the ON channel only). Pointing times are identified, and background fluctuations are evident in the integrated profile. Steps (1.2) to (1.4) do not apply to simulation data. The tests (3) are first performed on raw data (Figure 3c). The presence of intense interference causes the non-gaussian behaviour of the dispersion on ON ($\diamondsuit$) and OFF ($+$) dynamic spectra versus frequency resolution δf (with a slope -0.06, very far from the -0.5 expected for a gaussian noise). It also causes the very high ON/OFF correlation measured whatever δf. Figures 3d and 3e

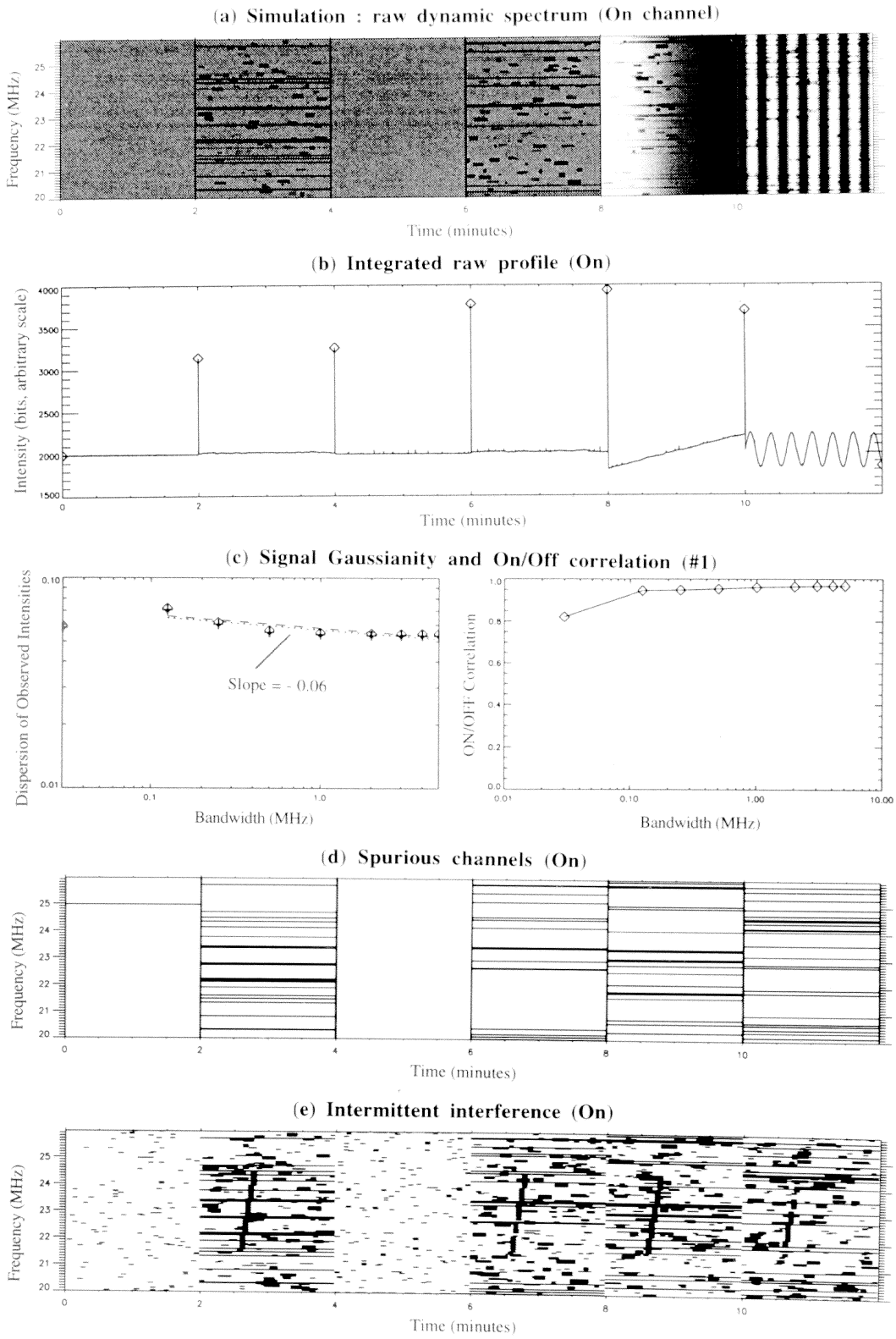

Figure 3: (a) Simulated dynamic spectrum containing weak broadband signal spikes and samples of all types of intense interference usually observed. (b, d, e) Main steps of interference identification and elimination. (c) Test of the efficiency of the cleaning of dynamic spectra. See section 6.2 for details.

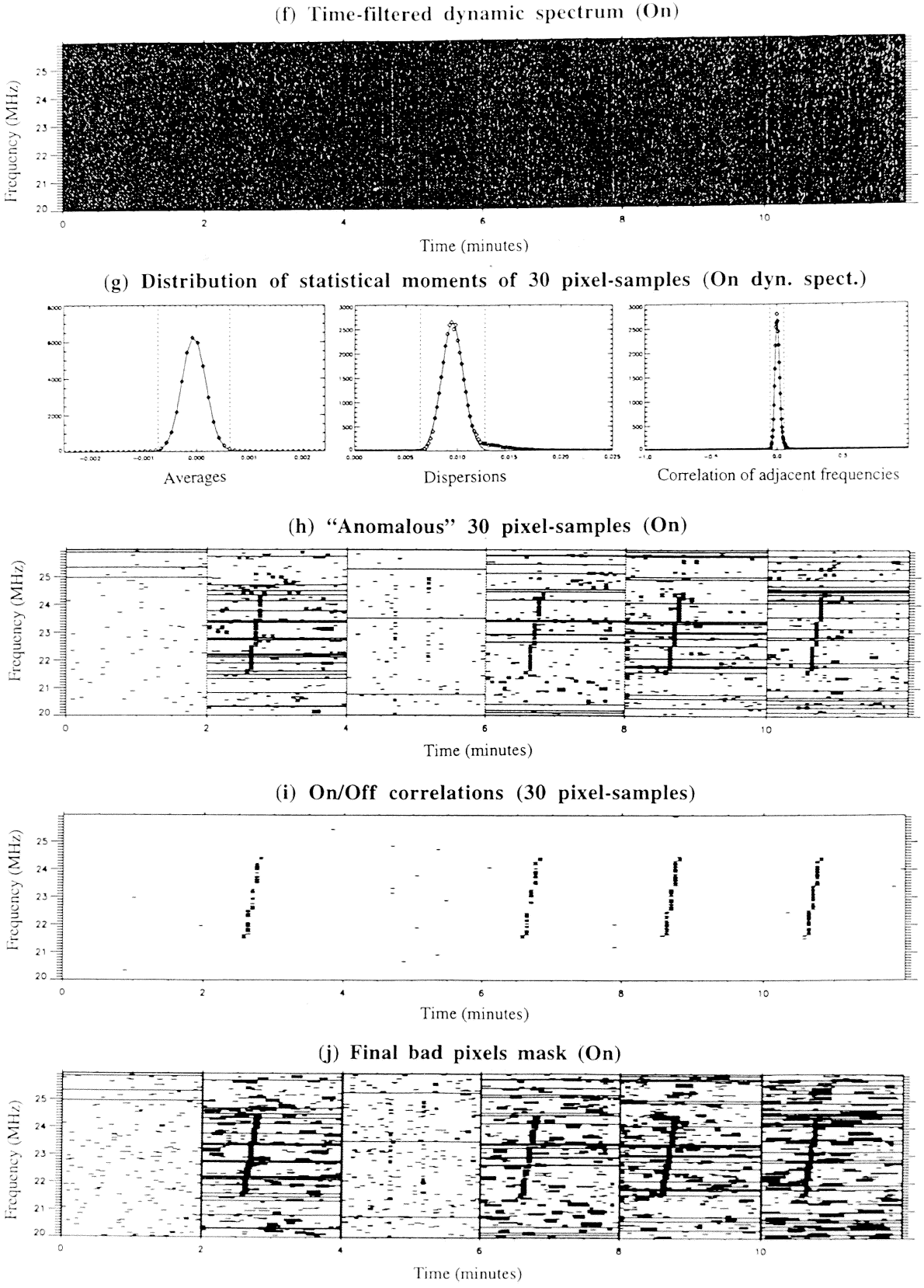

Figure 3: (f-j) Main steps of interference identification and elimination. See section 6.2 for details.

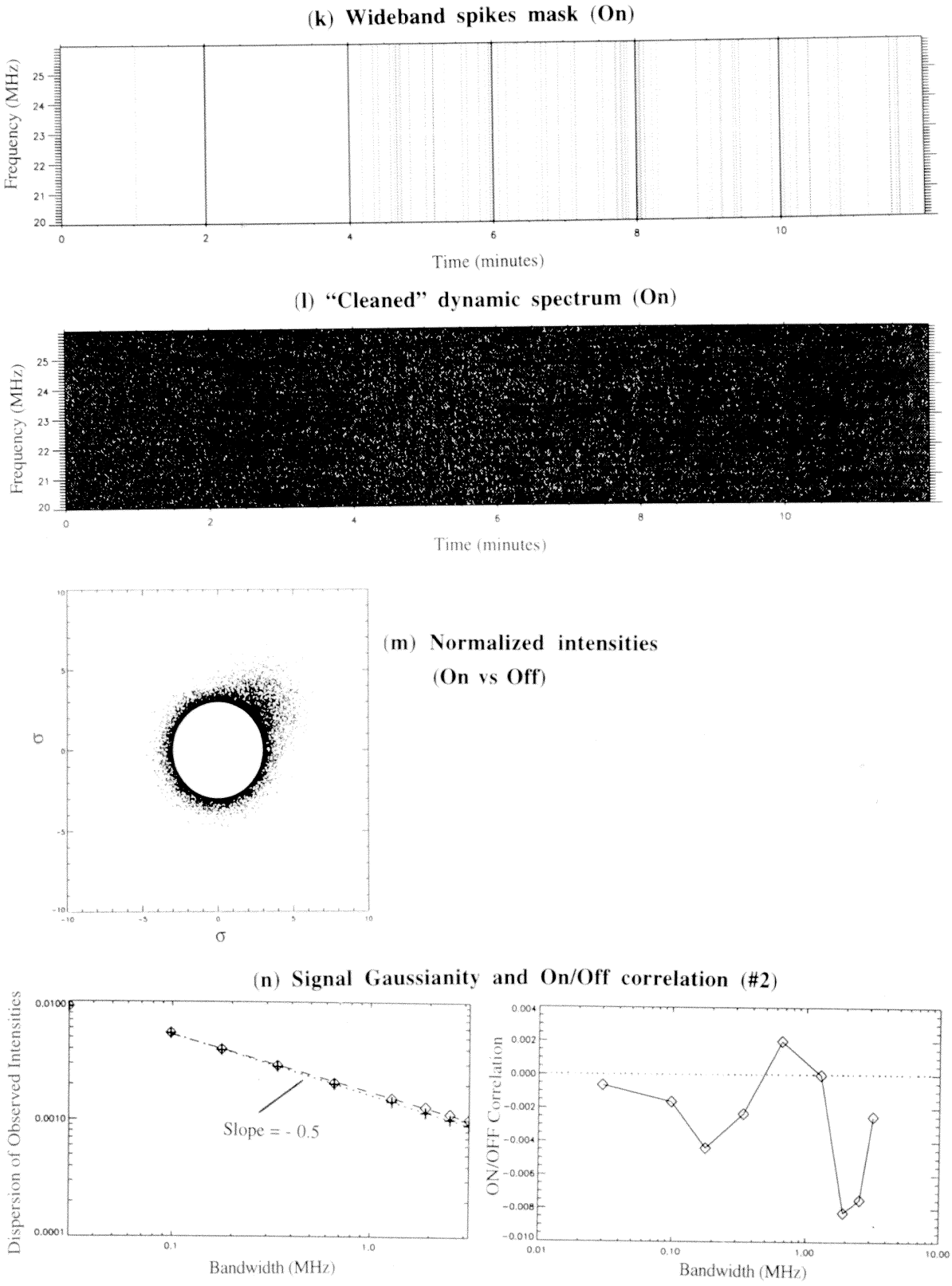

Figure 3: (k-m) Main steps of interference identification and elimination. (n) Test of the efficiency of the cleaning of dynamic spectra. See section 6.2 for details.

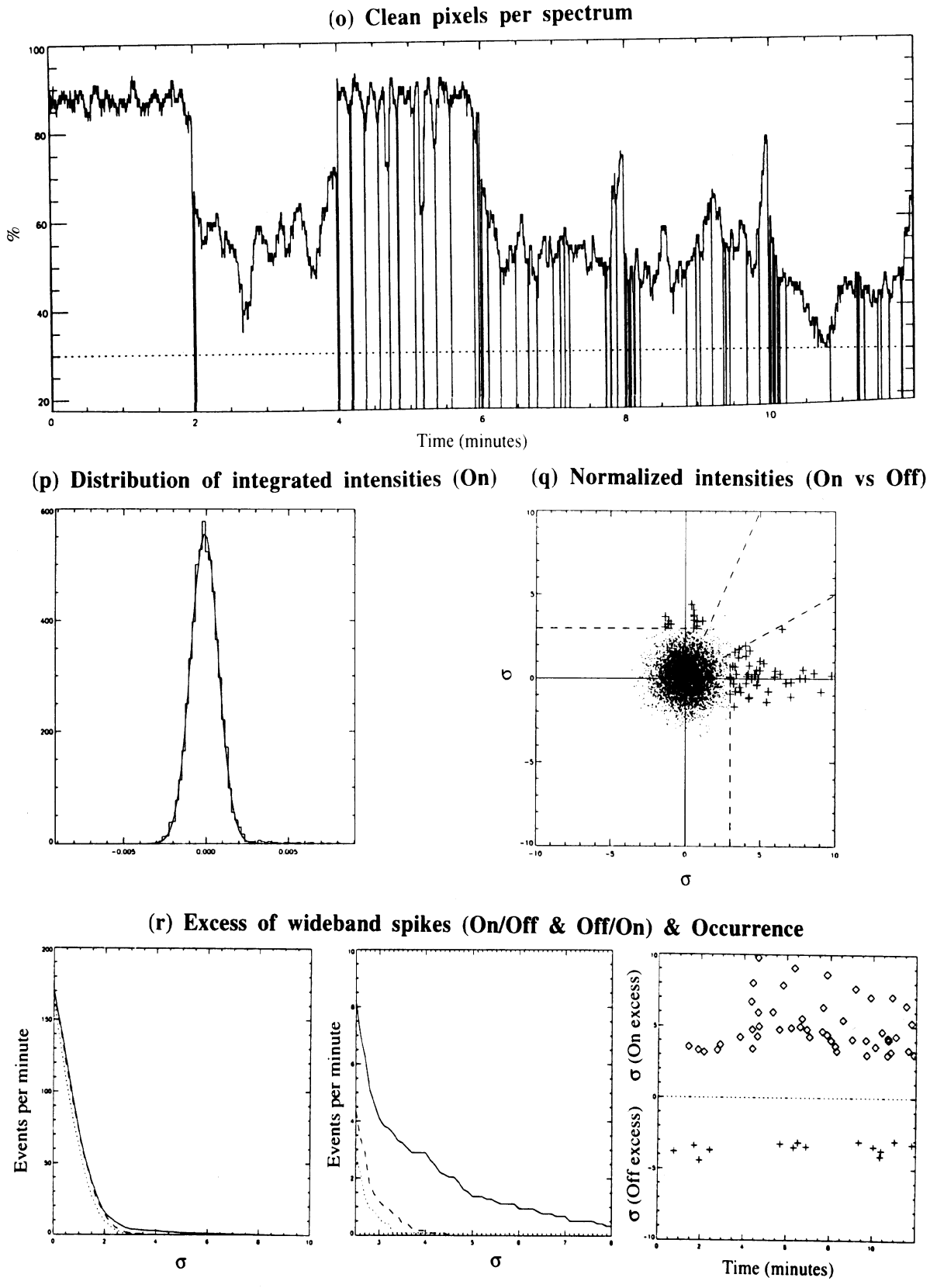

Figure 3: (o-r) Integration and broadband bursts detection. See section 6.2 for details.

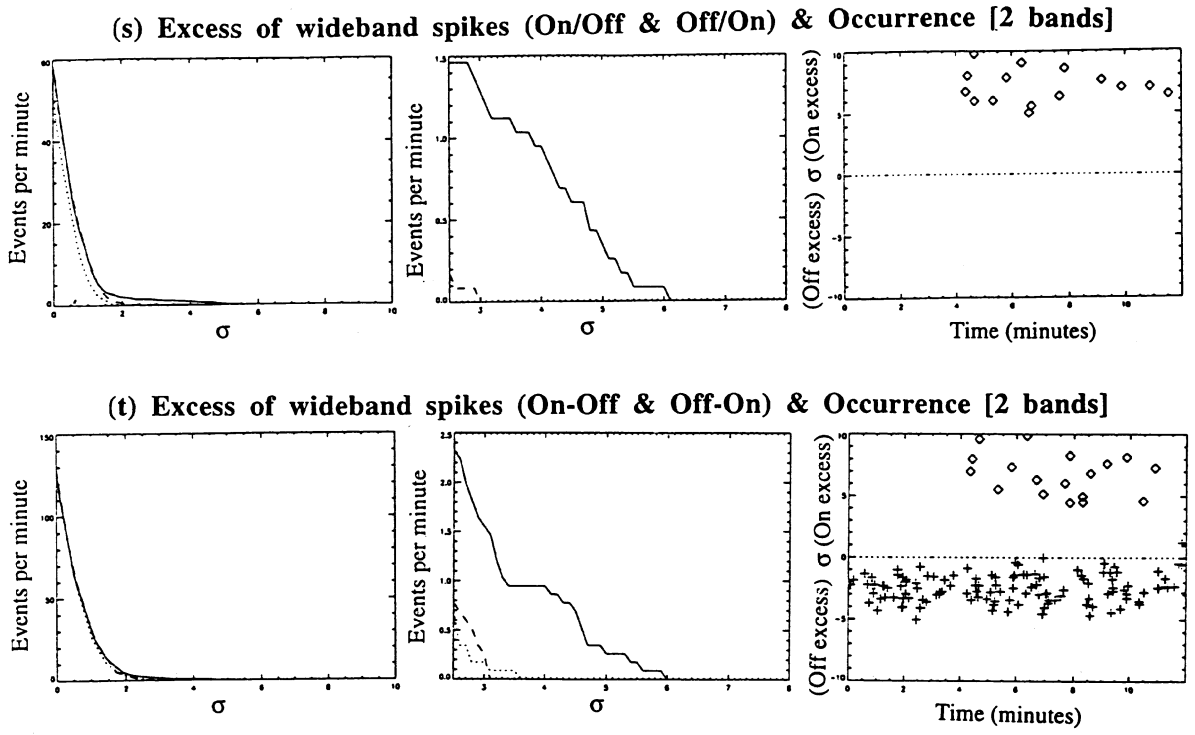

Figure 3: (s, t) Integration and broadband bursts detection. See section 6.2 for details.

illustrate step (2.1) of interference identification, displaying the maps of bad pixels (black parts) at timescales $\geq$ 2 minutes (spurious channels) and a few seconds (intermittent interference). Figure 3f characterizes step (2.3). The time-filtering greatly enhances the dynamic range of the plot, so that gaussian background fluctuations become visible. Figures 3g and 3h further illustrate step (2.1): the distribution of moments of 30-pixels samples (i.e. 1 frequency channel $\times$ 30 consecutive spectra) is analyzed, and samples with anomalously high values are considered polluted by interference. Step (2.2) is illustrated in Figure 3i, where the ON/OFF cross-correlation is analyzed on the same 30-pixels samples. Figure 3j is the final map of interference $m(f,t)$ resulting from two iterations of the whole procedure of interference identification, as described in (2.4). Figure 3k also results from step (2.1), giving the location of wideband spikes (interference and signal) detected in the ON dynamic spectrum. As expected, much less interference are detected in panels 1 and 3 (Figures 3d, e, h, i, j), while spikes are quasi-exclusively found in panels 3 to 6. Figure 3l displays the flattened, filtered ON dynamic spectrum after removal of the interference mapped in Figure 3j. The time filtering does not seem perfect, as background fluctuations are still visible in panel 6. The last step of the "cleaning" (2.4) is shown in Figure 3m, where each pixel considered as non-polluted in both the ON and OFF dynamic spectra is plotted as a dot, with coordinates being its normalized intensity (in units of σ) in the ON channel versus that in the OFF one (data points within the 3σ limit are omitted for clarity). Residual ON/OFF correlation is visible for high-intensity pixels (upper right part of the diagram). The pixels outside of the 3σ limit are then removed. The tests (3) are performed again on the cleaned dynamic spectra, and demonstrate the efficiency of the cleaning (Figure 3n): a slope of resp. -0.48 and -0.5 is found for ON and OFF

dispersions versus δf (the value -0.48 for ON is a first hint of the presence of broadband signal in it), and no residual ON/OFF correlation remains whatever the bandwidth of the frequency integration.

Figure 3o illustrates step (4.1), displaying the percentage of non-polluted pixels per spectrum. Below a minimum value of 30%, the corresponding spectrum is not retained in the final frequency-integrated time series. The resulting time series are computed with an average of $\sim$ 120 clean frequency channels per spectrum. Figure 3p shows the distribution of values of the resulting ON time series, which reveals an asymmetry (small high-intensity tail on the right of the diagram). The frequency integration has decreased the RMS dispersion from 0.01 (before integration) to $\sim$ 0.0009 (after), i.e. by the expected factor $(120)^{1/2} \approx 11$. The broadband bursts detection (step 4.2) is illustrated in Figures 3q and 3r: Figure 3q is a "dispersion diagram" similar to Figure 3m, but for values of the integrated ON and OFF time series. After renormalization, ON values corresponding to signal spikes (originally at $0.2 - 1\sigma$ level) can reach the 10σ level. Values above 3σ (ON or OFF) and higher than twice the other channel level (areas limited by dashed lines) are displayed as "+". The excess of high-intensity ON values at low OFF values, as compared to the symmetrical, is obvious. It is quantified on Figure 3r, which illustrates the discriminating statistics (4.2b): the number of ON events per minute above a given threshold (in σ) and higher than twice the corresponding OFF level is plotted against this threshold (solid line). The same statistics with ON and OFF exchanged is plotted as the dashed line. The dotted line is a reference curve, deduced from the same statistics applied to two purely gaussian time series. The center panel is a zoom of the left one, and shows that (i) the dashed line (OFF excess) is only 1 event/minute above the gaussian (minimum) false-alarm rate, and (ii) the solid line (ON excess) reveals a significant excess of ON spikes, corresponding to the signal searched for. The right panel gives the location (in time) of the peaks $> 3\sigma$ detected with ON ($\diamondsuit$) and OFF (+) excess. Most of the ON peaks are found, as expected, in the last 8 minutes of simulated data (panels 3 to 6). Finally, Figures 3s and 3t illustrate in the same way as Figure 3r the discriminating statistics (4.2b and 4.2c), performed after dividing the observation band in two (3 MHz each) and considering as significant only the signals detected in both bands (step 4.3). The same conclusions as above are obtained.

The simulations reveal that the various steps applied in the interference identification (and subsequent elimination) are very complementary to each other. None is enough alone to perform a satisfactory cleaning of the dynamic spectra. The following quantitative results are drawn:

- Through the whole procedure of interference identification (steps 2.1 to 2.4) $\sim 2.7 \times 10^5$ pixels (23%) are recognized as spurious in ON and OFF dynamic spectra separately (to be compared to the 1.4×10^5, or 12%, effectively put in the simulated data), with 9×10^4 in common (instead of 4×10^4), and a total of $\sim 4.5 \times 10^5$ (37%) for ON and OFF taken together (instead of 2.4×10^5, i.e. 20%).

- It is found that $\sim$ 100% of the interference put in the data are eliminated this way, by removing almost twice as many pixels from the dynamic spectra as those actually polluted (due to edge effects, gaussian noise peaks ...). The procedure designed to

remove intermittent interference (in step 2.1) is especially severe, eliminating > 2 times more data than necessary, but the fine tuning of the parameters used in each procedure has shown this to be necessary to ensure the efficiency of the difficult recognition/elimination of intermittent interference.

- About 50% too many broadband spikes (interference and signal) are also detected (Figure 3k). 60 signal spikes were put in the ON data (panels 3 to 6) at an intensity $\approx 0.2 - 1\sigma$ before frequency integration, i.e. $2.2 - 11\sigma$ after integration ($\times 120^{1/2}$) among which ~ 54 are expected at $> 3\sigma$ level. ~ 48 signal spikes have been detected in the simulation, of which $\sim 15\%$ are spurious (for example those detected in panels 1 and 2 of Figure 3a). The efficiency of signal detection is thus finally $> 75\%$.

- To quantify signal detection, the discriminating statistics (b) of step (4.2) appear the more effective. (c) leads to more noisy (but consistent) results (Figure 3t), and (a) and (d) are significant only if there remains no residual correlation in the data after interference elimination (Figures 3m, n).

- When performed in 2 bands (Figures 3s, t), the detection algorithm finds about 3 times less signal peaks, but the false-alarm rate (spurious or gaussian noise peaks) is reduced to ~ 0. This step (4.3) is less sensitive but useful as a check for the processing in a single band.

- Much more polluted data were also simulated, in particular including twice more spurious broadband spikes, each with intensity up to 10σ and time duration up to 5 consecutive spectra. However, similar results were found: about twice more pixels recognized as spurious compared to those actually put in the data, slope of -0.45 for the gaussianity test (step 3, Figure 3n), and only $\sim 50\%$ efficiency for signal spikes detection (instead of $> 75\%$). Results of the processing in 2 bands were almost identical to the previous ones, due to its greater immunity to interference and explicit use of the broadbandness of expected signal spikes.

The fact that $\sim 100\%$ of the simulated interference are eliminated by our procedure is encouraging, but does not prove that any kind of real interference (which can be extremely diverse) will be so. Simulation results are very promising, but our procedure still needs some improvements (especially the filtering and spikes detection) as well as additional fine tuning of the parameters used in the algorithms for interference identification. It can be noted than the whole processing involve heavy computation time, about 3 hours per observation (10000 recorded spectra) on a medium-size α-workstation.

7 Preliminary Results

By the end of 1996, only the data of the observation campaign #1 (2/1994) have been analyzed, as well as the Saturn observations of campaign #2 (5/1995, see Table 3). Interference elimination has been also checked on 51 Peg observations of campaign #3 (11/1995), but not yet dedispersed detection.

Analysis of the single-beam observations (ON only) of nearby stars during campaign #1 have been inconclusive, demonstrating the absolute necessity of simultaneous ON/OFF observations to eliminate spurious spikes.

Saturn observations of campaign #1 have been performed using a swept-frequency analyzer (section 5.4), on the 31/1, 1/2 and 5/2/1994. Broadband spikes appear in this case as consecutive intense pixels randomly positioned in frequency, depending on their time of occurrence relative to the receiver's sweeping cycle (cf. Zarka, [1985b]). Analysis of the observation of 1/2/1994 ($\sim$ 2 hour total duration, using the NS array, alternatively ON Saturn and OFF Saturn every 4 minutes, with $\delta f = 300$ kHz and $\delta t = 25$ msec per measurement i.e. a $1\sigma = 25$ Jy sensitivity) has revealed - after floating background substraction, elimination of high-intensity pixels, and selection of events lasting for ≥ 75 msec - a significant excess of ON events (~ 190) versus OFF events (~ 50). This excess of 140 events/hour = 2.3 events/minute above the 25 Jy level is consistent with estimates of section 2, and could be attributed to the detection of Saturn's lightning. No excess was found for the two other observations, for which the EW array (of smaller A_e) was used and the data were more polluted by interference.

All other previous attempts to detect SED had led to negative results. Those include:

- Early observations by Barrow in 1967 (personal communication) at $16 - 18$ MHz, with narrow bandwidth, using the Arecibo dish,
- Observations by Carr et al. (observatory report, 1982), using the Maipu ($A_e = 6000$ m^2, with $\delta f = 3$ MHz at $f = 45$ MHz and $\delta t = 30$ msec, i.e. $\sigma = 30$ Jy) and Florida ($A_e = 8000$ m^2, with $\delta f = 500$ kHz at $f = 26.3$ MHz and $\delta t = 30$ msec, i.e. $\sigma = 280$ Jy) arrays,
- Observations at 21 cm wavelength with the Nançay radiotelescope during the Voyager 2 Saturn flyby [Lecacheux and Biraud, 1984].

These non-detections can be attributed to the limited effective areas and observation bandwidths used and to the steepness of the SED spectrum towards high frequencies (1 GHz). However, it should be kept in mind that Saturn's atmospheric storm activity is also very variable at the timescale of months, as it was discovered during Voyager 1 and 2 flybys (separated by 9 months), and confirmed by the apparition of a bright equatorial storm system in 9/1990 and its subsequent evolution as a complex planetary disturbance affecting the whole equatorial region a month later [Sanchez-Lavega et al., 1991]. This activity may be seasonal, linked to solar heating variations for example. Storms seem to appear preferably in equatorial regions, where the winds are strongest and where temperature gradients may exist at the edges of the rings' shadow.

Processing of observations of campaigns #2 and #3 has shown that dynamic spectra are much cleaner after interference elimination, as proved by the gaussianity test for which we find a dispersion decreasing in $\delta f^{-0.45}$ (very close to the $\delta f^{-0.5}$ expected for a gaussian noise) for the majority of data files. 10 to 30% of the spectra are eliminated through the processing (steps 1.1, 1.4, and 4.1 for spectra containing $\leq 30\%$ of non polluted pixels), and 30 to 60% of the frequency channels (steps 1.3 and 2). Finally, 40 to 70% of the

pixels in ON and OFF dynamic spectra are considered as spurious. Frequency integration is expected to increase the S/N ratio by a factor $\sim 6-7$ (between the 130 kHz band of each AOS frequency channel and the final $5-6$ MHz clean band). In practice, a factor 3 to 6 is obtained, depending on the initial degree of pollution of the observations. The corresponding sensitivity achieved is $2-4$ Jy (1σ) for 51 Peg observations (~ 12 Jy before frequency integration), and $3-6$ Jy for Saturn observations (~ 20 Jy before integration). The best observational time is found to be between 0h and 5h Local Time. Out of these limits, data files are so much polluted that our procedure does not perform well (due to strongly biased statistics).

In some of the processed Saturn files (5 out of 14, campaign #2), we obtain no significant excess in either ON or OFF channel, and the number of detected peaks is close to or slightly above that expected for gaussian noise (corresponding to $\sim 1-2$ peak/minute above the 3σ level for Saturn observation parameters). The same result was obtained for the 8 processed 51 Peg files of campaign #3. However, a statistically significant excess of peaks in the ON channel was found for $\sim 50\%$ of clean Saturn files (the acquisitions not too polluted initially, representing 10 files out of 14), at a level of up to 2 events/minutes (3σ). An excess in the OFF channel was found for $\sim 10\%$ of clean files up to the same level, and no excess in the remaining 40% of clean files. The succession in time of ON excesses during the 4 consecutive nights of Saturn's observations (14–17/5/1995, i.e. ~ 8 Saturnian rotations of $\leq$ 10h39.4min) is not inconsistent with an equatorial source, but still needs to be confirmed. The false-alarm rate achieved ($\sim$ gaussian) is significantly less than the number of peaks expected from Voyager 1 and 2 estimates for Saturn's lightning signals, which strongly suggests that their detection is possible in the present state of the observation procedure and with minor improvements of the processing. The analysis of the 58 Saturn acquisitions of campaign #5, spread over 9 consecutive nights close to opposition, should allow us to conclude about the current presence or absence of lightning storms in Saturn's atmosphere.

For the analysis of 51 Peg observations, dedispersed frequency-integration and detection should be more effective and increase interference immunity (because spurious spikes will be dispersed before integration). The results of interference elimination for 8 files of campaign #3 are encouraging, but much more reliable results are expected from the final analysis of the 30 acquisitions of campaign #5 (also spread over 9 consecutive nights near opposition, covering 2 revolutions of 51 Peg B around its parent star!).

8 Conclusions and Perspectives

The above results show that the ground-based search for solar system planetary lightning and exoplanetary radio bursts at decameter wavelengths is far from unrealistic.

In case of detection of radio bursts from the environment of a nearby star, the first question will be: "Does they come from the star itself or from a planet orbiting it?". The angular resolution available does not allow to answer this question. Possible ways are:

- Polarization measurements: planetary auroral radiations are much more strongly

circularly or elliptically polarized than solar radio bursts (possibly due to the complex small-scale topology of the solar magnetic field which causes a mixing of the polarization of several small-scale sources); however, no decameter radiotelescope possesses presently both a very large area and polarization measurement capability.

- Long-term (days-weeks) monitoring of the radio bursts, and spectral analysis of their occurrence in search for periodicities revealing the planet's rotation period (hours rather than weeks for solar-type stars). For planets very close to their parent star (like 51 Peg B), the rotation period is likely to be equal to the orbital period.
- Motivating other observations, with different methods (spectroscopy/radial velocity measurements, astrometry, occultations, IR imaging ... cf. Schneider, [1997]).

Informations that can be obtained from radio detection of exoplanetary radio bursts (in addition to the existence of the planet itself) are thus: existence of the planet's magnetic field and estimate of its magnitude, output radio power and its fluctuations with time, rotation (and possibly orbital) period. If successful, this research program could initiate comparative exo-magnetospheric physics. Brown dwarf detection is a-priori not excluded from this program, although nothing is known (and thus expected) about the possible production of radio bursts by these objects.

In its concluding remarks to the "Planetary Radio Emissions III" conference, B. F. Burke [1992] outlined a way for future planetary radio emission studies, axed on the radio search for exoplanetary systems. In his truly "visionary" paper, he mentioned the possibility of discovering and studying exoplanetary magnetic fields and magnetospheres, and the necessity to use large decameter radiotelescopes like UTR-2 and to develop proper signal processing to achieve a large bandwidth. He also discussed the existence of much stronger radio bursts than Jupiter's ones, and the possibility to measure planetary rotation and possibly orbital periods through the monitoring of their radio emission. However, this future he outlined was at the horizon of $20 - 30$ years. In the course of 5 years, through our French/Ukrainian/Austrian collaboration, we begin to try to turn this dream into a hope.

The perspectives for the near-future include:

- The systematic search with UTR-2 for exoplanetary radio bursts around all target stars closer than $\sim$ 25 pc (i.e. with $\delta \geq -10°$, and preferably single and close to solar spectral type); this program can be realized in $2 - 3$ years with the AOS and data-archiving system (CD-Rom) presently operating at UTR-2. It should at least provide upper limits for planetary radio outputs up to 25 pc distance.
- The use of a digital receiver [Kleewein et al., this volume] in addition/replacement of the AOS. It will provide a higher dynamic range (> 60 dB) improving the interference immunity and the efficiency of the data processing, and a better stability possibly allowing for the search of auroral radio emissions slower than Jovian S-bursts.

- Observations in correlation mode (NS × EW) at UTR-2, which have been first tested during campaign #5, in order to reduce the confusion affecting the observations and their susceptibility to interference.
- Possible improvement of UTR-2's immunity to interference (through adaptative filtering, for instance - see Denis and Zarka, [1996]).
- Observations at meter wavelengths (for example using the new Indian GMRT, [Swarup, 1990], less polluted by man-made interference and terrestrial lightning, but requiring the existence of very intense exoplanetary magnetic fields.

The far-future perspectives include:

- Upgrade or construction of a giant ground-based decameter array (with effective area of the order of 1 km^2); several projects are presently under study.
- Projects of radio observations from the far side of the moon (although no radiotelescope with a large enough effective area is presently planned).
- Searches at lower frequencies, below the galactic background peak (kilometer wavelengths); those would be more sensitive, due to the lower sky background temperature, but must be conducted above the Earth's ionosphere and suffer more from propagation effects like temporal dispersion and broadening. Burke [1992] suggested that pre-planetary systems could produce such low-frequency radioemissions.

In the course of exoplanetary radio search, the general-purpose methods we developed for interference identification, cleaning of dynamic spectra, and bursts detection, can be applied to the study of other weak decameter radiosources (flare stars, pulsars ...) and may constitute an opening of the radio decameter window, otherwise quite "closed" by the high-level of electromagnetic pollution. However, those methods are still not perfect, and their output should be analyzed with caution. If, according to Burke [1992] "Every planet presents surprises", we should keep in mind that "Every surprise [that could come out of the analysis of dynamic spectra] does not hide a planet".

Acknowledgements: The authors acknowledge support from the E. C. INTAS program (contract for Joint Research Project #94-1296). V. B. Ryabov acknowledges support from NATO (Scientific Fellowship program).